Article

Anomalous Pressure-Resilient Thermal Conductivity in Hybrid Perovskites with Strong Lattice Anharmonicity and Small Bulk Modulus

Jin Yang, Ankit Jain, Liwu Fan, Yee Sin Ang, Hanying Li, and Wee-Liat Ong*

Read Online

ACCESS | Metrics & More | Article Recommendations | SI Supporting Information

ABSTRACT: The pressure-enhanced electronic properties of metal halide perovskites are advantageous for photovoltaic and thermoelectric applications. However, another critical performance factor, the thermal conductivity behavior under pressure, has received much less attention. Using the state-of-the-art phonon Wigner transport equation, we studied the prototypical methylammonium lead triiodide in its cubic phase (c-MAPbI$_3$) to discover a new anomalous pressure effect, where the dominant coherence-channel thermal conductivity is invariant with changing pressure. The straightening of the octahedra and the shortening of the lattice constant with increasing pressure help create this anomalous behavior that suppresses the overall thermal conductivity changes. By comparing with the bulk modulus and Grüneisen parameter of several materials, we unveil another unusual phenomenon in c-MAPbI$_3$. The thermal conductivity of this soft and strongly anharmonic material under pressure behaves like those of stiff and weakly anharmonic materials. Together with the reported enhanced optoelectronic properties, our findings support MAPbI$_3$ as a pressure-modulated energy conversion material with decoupled thermal and electrical properties.
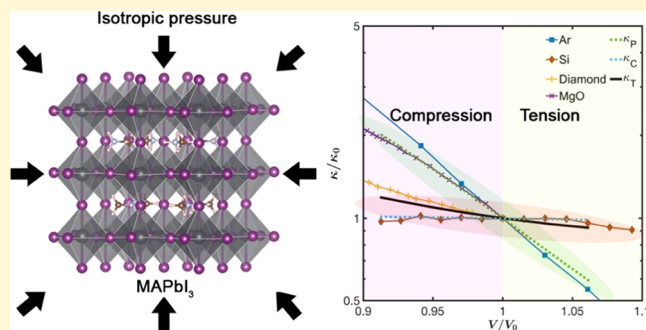
1. INTRODUCTION

Metal halide perovskites, especially the methylammonium lead triiodide (MAPbI$_3$), with their high absorption coefficient, low thermal conductivity, and low-cost solution processing,[1−5] have attracted interest from the solar cells, nanoelectronics, and thermoelectrics communities. Accessible external fields like pressure can further regulate their optoelectronic properties by affecting their crystal structures, resulting in vastly enhanced stability and power conversion efficiency.[6−8] For example, Qiao et al.[8] applied compressive and tensile strains in MAPbI$_3$ that eliminated the defect-induced trap states and prolonged the recombination time of carriers to create better-performing solar cells. However, the modulation effect of pressure on the nanoscale thermal transport properties of MAPbI$_3$, which often impact the performance and efficiency of energy conversion devices, has received far fewer investigations.[9−11]

To date, different pressure studies on the thermal conductivity of MAPbI$_3$ have yielded inconsistent results. Gao et al.[9] assessed the thermal conductivity of a pseudocubic MAPbI$_3$ (c-MAPbI$_3$) crystal using the Green-Kubo equilibrium molecular dynamics (EMD) method with the ab initio-derived MYP empirical potential.[12] They found that its thermal conductivity at the temperature of 350 K increases from around 0.4 to 0.6 W m^{-1} K^{-1} when pressure rises from 0 to 10 GPa. However, another independent theoretical study using

the same method and potential predicted an almost tripled thermal conductivity for c-MAPbI$_3$ at 10 GPa to around 1.5 W m^{-1} K^{-1}.[10] Lastly, with a similar simulation setup on a tetragonal MAPbI$_3$ at room temperature, Rahman et al.[11] investigated the effects of applying a uniaxial tensile strain along the a-direction (lattice constants $a = b \neq c$) on its thermal conductivity. The accompanying compressive strain is negligible along the b-direction but significant along the c-direction. They found that, in the elastic stress−strain region, the applied uniaxial tensile strain decreases the thermal conductivity along the stretched a- and the unchanged b-directions, but has little effect along the compressed c-direction. These results suggest rather complex pressure-induced thermal conductivity changes in MAPbI$_3$ that require a deeper structure−property investigation.

Although the above molecular dynamics (MD) studies[9−11] have provided some preliminary insights, the phonon properties of c-MAPbI$_3$ are still lacking. An in-depth understanding of these thermal carriers is required to harness an external field
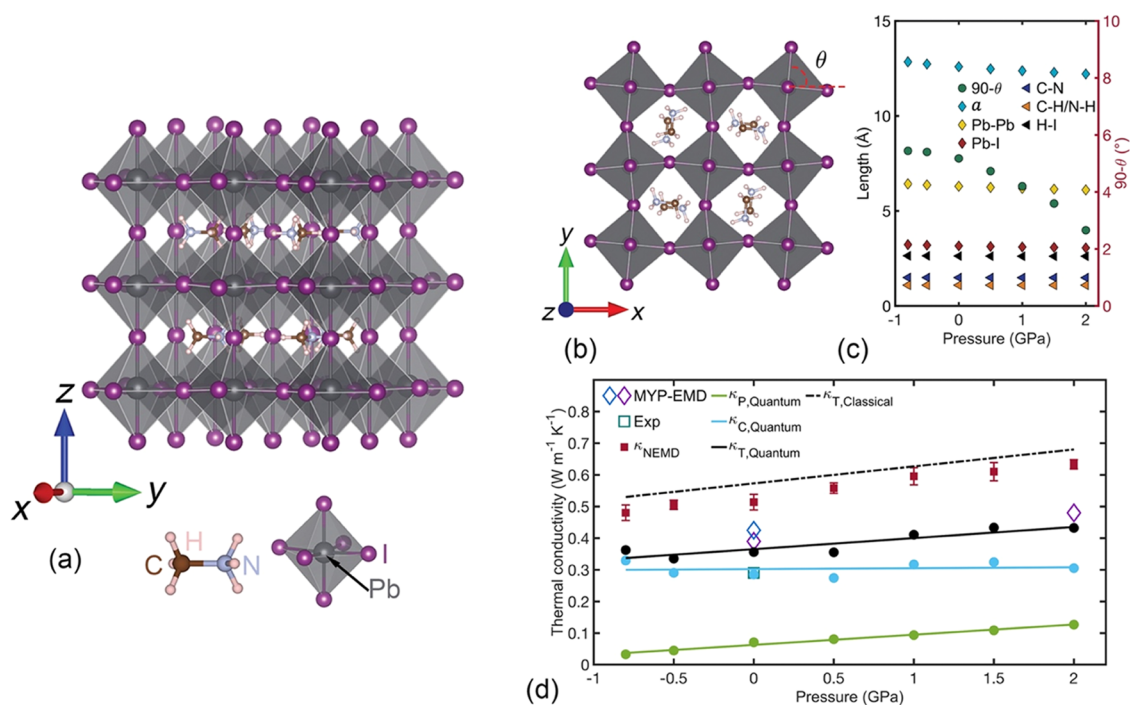
Figure 1. (a) Optimized three-dimensional structure of c-MAPbI$_3$ at 0 GPa. (b) An $X-Y$ view of the optimized structure shows the arrangement of the MA cations and tilt angle $(90 - \theta)$ of an octahedron with θ measured from the horizontal axis. (c) Changes in the structural parameters of the c-MAPbI$_3$ unit cell with 96 atoms, including the tilt angle $(90 - \theta)$, lattice parameter (a), and bond length of Pb–Pb, Pb–I, I–I, C–N, C–H, N–H, and H–I versus pressure. (d) Variations of thermal conductivity of c-MAPbI$_3$ at a temperature of 350 K versus pressure. The error bars of the NEMD results denote the standard errors from five independent runs. The Exp[28] and MYP-EMD[9,22] are experimental and theoretical equilibrium molecular dynamics (EMD) results from the literature using the first-principles-derived potentials.[12] All structures are visualized using VESTA.[29]

for regulating thermal transport effectively. As such, alternative techniques like the lattice dynamics (LD) method are needed to elucidate the effect of an external field on the phonon modal heat capacity (C_λ), group velocity (v_λ), and lifetime (τ_λ).[13−16] A thorough understanding of these properties is also critical for manipulating thermal transport through nanostructuring.[3,13,17] Used together with the phonon Boltzmann transport equation (PBTE),[18] it is known that pressure affects thermal conductivity through a complex interplay between the above modal properties.[13] However, the PBTE intrinsically assumes the validity of the phonon gas model and can only account for thermal conductivity contributions from the phonon particle-nature (aka population-channel, κ_P).[19,20] This approach is inadequate for complex crystals like MAPbI$_3$ with its multiple overlapping phonon branches and an intrinsic thermal transport dominated by contributions from the phonon wave-nature (aka coherence-channel, κ_C).[21−23]

Here, we instead combined lattice dynamics with the state-of-the-art phonon Wigner transport equation (LD-PWTE)[19,20] to probe the pressure effects on κ_P and κ_C in the cubic phase MAPbI$_3$ (c-MAPbI$_3$). The c-MAPbI$_3$ phase is common in MAPbI$_3$-based devices like photovoltaics and thermoelectrics operating above room temperatures. The LD-PWTE arises from the unified theory of thermal transport[19,20] that provides a comprehensive understanding of the nanoscale thermal transport behaviors and accounts for the crystal−glass duality. The thermal conductivity calculated from the LD-PWTE is contributed by the phonon population-channel (κ_P) and the phonon coherence-channel (κ_C) and reduces to the result from the phonon Boltzmann transport equation at the simple crystal limit (κ_P) or from the Allen−Feldman (AF) theory at the harmonic glass limit (κ_C).[19,20] Nonequilibrium molecular

dynamics (NEMD) was also performed to complement our PWTE calculations. We found that the κ_C is anomalously pressure-invariant, while κ_P raises from 0.033 to 0.127 W m^{-1} K^{-1} with pressure increasing from −0.8 to 2.0 GPa. Every phonon mode contributes more to the total thermal conductivity (κ_T) with increasing pressure, with more modes switching their contributions from κ_C to κ_P. A quick comparison with other widely studied materials using the bulk modulus and Grüneisen parameter unveiled a new anomalous pressure-mitigating effect from κ_C on the overall thermal conductivity. Our results show that a dominant κ_C in complex crystals imparts new physics to their thermal transport behavior under pressure.

2. RESULTS AND DISCUSSION

All simulations and calculations in this study employed the ab initio-derived MYP empirical potential[12] with details summarized in the Section 4. The pressure effect on the thermal conductivity of c-MAPbI$_3$ was studied at a low-to-moderate pressure range from −0.8 to 2.0 GPa (minus sign indicates tension) to exclude the possible uncertainties from the empirical potential at higher pressures.[24] The optimized stable unit cells at different pressures, each with 96 atoms (Figures 1a, b and S1), were obtained using a recently proposed structural optimization method to perform lattice dynamics calculations.[21] These structures have a space group of $I/4m$. Our MD results at the temperature of 350 K suggest that c-MAPbI$_3$ undergoes a phase transition when the compressive stress is higher than 2.0 GPa (Figure S1). Also, the magnitude of the applied tension was restricted to below 0.8 GPa as the stimulated structures became amorphous and disintegrated at
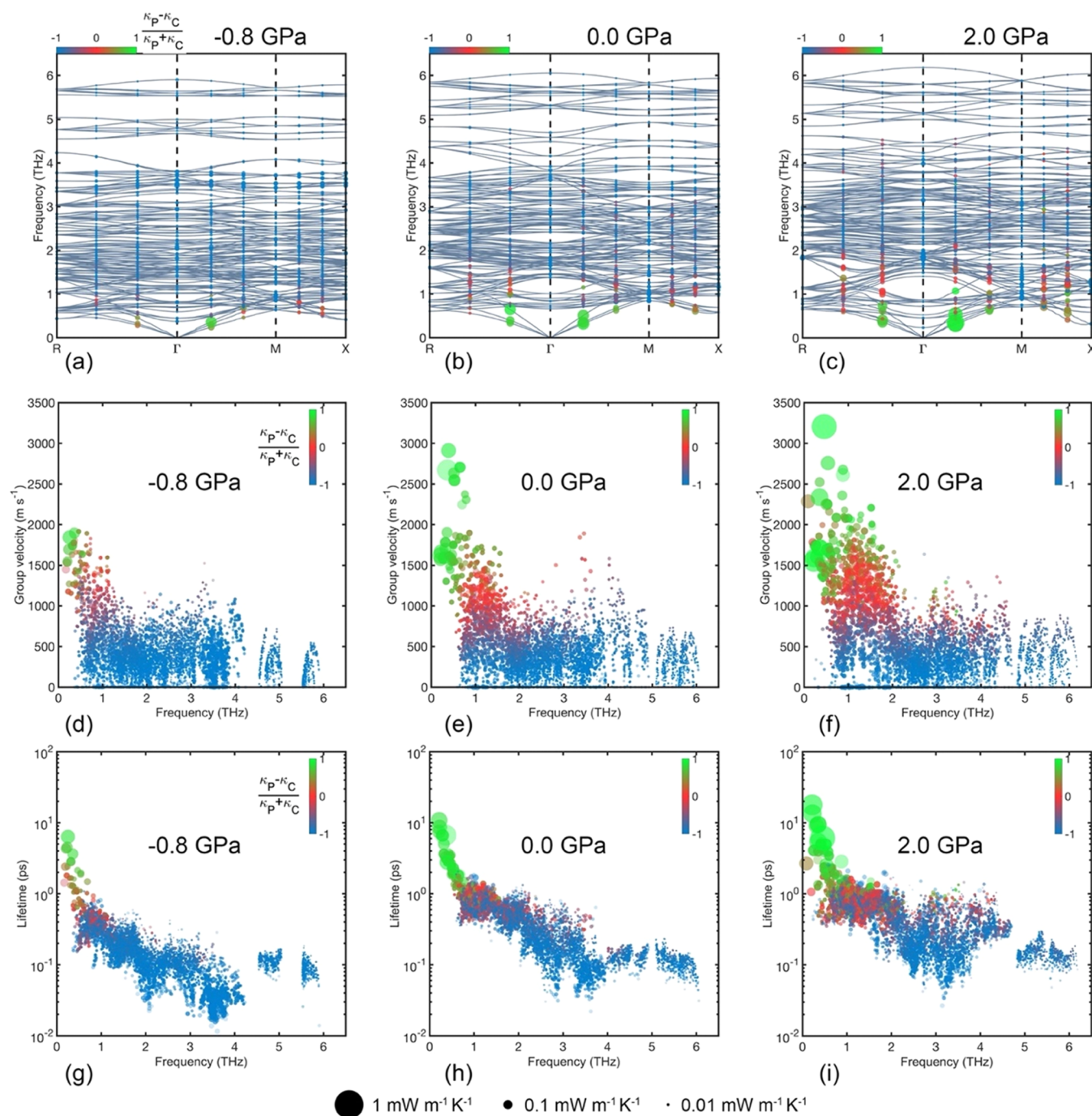
Figure 2. Modal phonon properties of c-MAPbI$_3$ at three different pressures, −0.8 GPa (left column), 0.0 GPa (middle column), and 2.0 GPa (right column) with (a−c) the phonon dispersion, (d−f) group velocity, and (g−i) lifetime. The colored circles represent the sampled phonon modes in the Brillouin zone (BZ). The area of each circle indicates the thermal conductivity contribution from a specified phonon mode. Its color depicts the proportional contribution to each channel. Light green indicates 100% contribution to the population-channel (κ_P), light blue indicates 100% contribution to the coherence-channel (κ_C), and red indicates equally to both channels. Each κ_C value is distributed to the pair of contributing phonons according to their heat capacity values.[19,20] Note that the phonon properties with frequencies above 6.5 THz are not shown for clarity, as their contributions are insignificant (see Figure S5).

higher tensile stresses. These phase transitions are related to phonon softening,[14,15] which will be discussed later.

As these structural transitions are intimately related to the phonon properties,[21] we examined how the structure evolved from −0.8 to 2.0 GPa. As illustrated in Figure 1c, the bond lengths between the inorganic atoms (i.e., Pb−Pb, Pb−I, and I−I) decrease by around 5% as the pressure increases from −0.8 to 2.0 GPa. On the other hand, the bond lengths in the

organic cations remain nearly consistent, depicting a weak effect on the MA cations by the applied pressure. The above bond length changes culminated in a decrease in the lattice constant (a) by 0.23 Å with an increase of 1 GPa. Another observable change is the decrease in the tilt angles (90 − θ) (Figure 1b,c) that straightens the inorganic framework at higher pressures. Further, changes in the tilt angle also affect the relative atomic positions in the c-MAPbI$_3$, which adds an

extra degree of calculation complexity not present in previous pressure studies on simple atomic crystals.[15,25−27]

From Figure 1d, our size-converged NEMD thermal conductivity (κ_{NEMD}) at the temperature of 350 K displays a gentle upward trend with increasing pressures. This trend agrees with results from previous theoretical studies[9] and coincides with our LD-PWTE total thermal conductivity value under classical statistics ($\kappa_{T,Classical}$). This agreement is further discussed below. The LD-PWTE total thermal conductivity calculated using quantum statistics ($\kappa_{T,Quantum}$) displays a similar trend, with its value at 350 K and 0 GPa agreeing with previous experimental[28] and theoretical[9,22] results. Our results depict that the coherence-channel dominates the MAPbI$_3$ thermal conductivity. Its contribution, however, drops from 89 to 71% when the pressure is increased from −0.8 to 2 GPa.

Surprisingly, the coherence-channel thermal conductivity value ($\kappa_{C,Quantum}$) is almost pressure-invariant from our LD-PWTE calculation. This trend is not seen in past pressure-dependent thermal conductivity studies for other dielectric crystals or amorphous materials with large coherence-channel contributions.[30] The rise in population-channel thermal conductivity ($\kappa_{P,Quantum}$) accounts for the increase of $\kappa_{T,Quantum}$ as pressure grows. With the MAPbI$_3$'s Debye temperature[31] at 120 K, the lower value of $\kappa_{T,Quantum}$ than $\kappa_{T,Classical}$ at the temperature of 350 K indicates that the use of classical statistics is unsuitable. Several reasons are possible, including the significant coherence-channel contribution by the active high-frequency optical phonons under classical statistics[21] and the ill-defined phonon lifetime in classical statistics-based LD calculations.[32] Hence, only results from quantum statistics calculations are discussed below.

To shed light on how changes in the structure affect the thermal transport mechanism, the phonon dispersions under three pressures (i.e., −0.8, 0.0, and 2.0 GPa) were calculated and plotted in Figure 2. Figures 2a−c and S2 depict that certain phonon modes below 1 THz soften near the Γ, M, and X points when MAPbI$_3$ is pulled to −0.8 GPa or compressed to 2.0 GPa. The softening near these Brillouin zone points indicates a phase transition,[14,15] agreeing with our MD results (not shown). On the other hand, in the case of 2.0 GPa, phonon branches below 2 THz, especially the acoustics ones, stiffen to produce higher phonon group velocities. As evident from Figure 2d−f, the highest group velocity rises from less than 2000 m s^{-1} to around 3200 m s^{-1} with increasing pressure. This rise comes from a more closely packed unit cell with shorter Pb−Pb and Pb−I bonds (Figure 1c) that stiffen the phonon branches (see phonon density of states in Figure S3). Also, the hydrogen bond length in the (N−H$_3$)−I, related to the coupling between a MA cation and the cage formed by the inorganic octahedra,[33] is almost constant within the investigated pressure range. This invariant hydrogen bond length is a consequence of the almost fixed average cage length along the stiff C−N bond direction (i.e., p in Figure S4). However, the other average cage dimensions (i.e., a, b, and c in Figure S4) shrink with increasing pressure and constrain the MA cation's motion, resulting in a smaller anharmonicity that enhances the phonon lifetime (Figure 2g−i).

The above structural changes switch a small number of phonon modes, mainly the low-frequency acoustic branches from the inorganic octahedra,[21,34] to contribute predominantly to from κ_C. More specifically, when compressing from −0.8 to 2.0 GPa, the number of phonon modes contributing predominantly to the population-channel [i.e., $(\kappa_P − \kappa_C)/(\kappa_P$

$+ \kappa_C) > 0.5$] increases about 12 times from 0.08 to 0.97%. This increase induces the κ_P to rise from 0.033 to 0.127 W m^{-1} K^{-1}. Although the number of phonon modes contributing predominantly to the coherence-channel [i.e., $(\kappa_P − \kappa_C)/(\kappa_P + \kappa_C) < −0.5$] decreases by 8.55% from 47.75 to 39.21%, they still dominate. The remaining phonon modes contribute to both the κ_P and κ_C.

The average transport-related parameters can provide a more qualitative and easier understanding of the changes in the modal-based phonon properties under pressure. For κ_P

$$\kappa_P^\alpha(\boldsymbol{q})_s = C(\boldsymbol{q})_s |v^\alpha(\boldsymbol{q})_s|^2 \tau(\boldsymbol{q})_s \tag{1}$$

where $\boldsymbol{q}$ and s indicate a wavevector and a phonon branch. α is one of the Cartesian directions, $C(\boldsymbol{q})_s$ is the volumetric specific heat of a phonon mode, $v(\boldsymbol{q})_s$ is the phonon group velocity, and $\tau(\boldsymbol{q})_s$ is the phonon lifetime. As shown in Figure 3a,
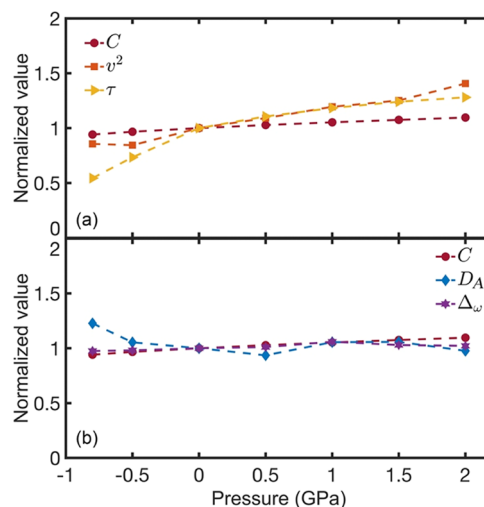

Figure 3. Average phonon properties are normalized with the values at 0 GPa for the (a) population-channel (κ_P) and (b) coherence-channel (κ_C). C is the mode-averaged heat capacity, v^2 is the mode-averaged squared group velocity, and τ is the mode-averaged lifetime. D_A is the mode-averaged anharmonic modal diffusivity, and Δ_ω is the average interband spacing.

consistent with the above modal analysis, the increase in κ_P comes mainly from the rise in the mode-averaged group velocity and lifetime, with a small contribution from the heat capacity increase.

For κ_C, we extracted an anharmonic modal diffusivity term, $D_A(\boldsymbol{q})_s$, from the PWTE formulation[20] and plotted it in Figure 3b. Here

$$D_A^\alpha(\boldsymbol{q})_s = \sum_{s' \neq s} \left\{ \frac{1}{2} \frac{\omega(\boldsymbol{q})_s + \omega(\boldsymbol{q})_{s'}}{C(\boldsymbol{q})_s + C(\boldsymbol{q})_{s'}} \left[\frac{C(\boldsymbol{q})_s}{\omega(\boldsymbol{q})_s} + \frac{C(\boldsymbol{q})_{s'}}{\omega(\boldsymbol{q})_{s'}} \right] \right\}$$
$$|v^\alpha(\boldsymbol{q})_{s,s'}|^2$$
$$\left(\frac{\frac{1}{2}[\Gamma(\boldsymbol{q})_s + \Gamma(\boldsymbol{q})_{s'}]}{[\omega(\boldsymbol{q})_{s'} − \omega(\boldsymbol{q})_s]^2 + \frac{1}{4}[\Gamma(\boldsymbol{q})_s + \Gamma(\boldsymbol{q})_{s'}]^2} \right) \tag{2}$$

where s' and s indicate modes from different phonon branches, $v(\boldsymbol{q})_{s,s'}$ is the off-diagonal phonon group velocity, and the other terms are as defined for eq 1. The expression in the curly brackets is dimensionless and distributes the coherence-
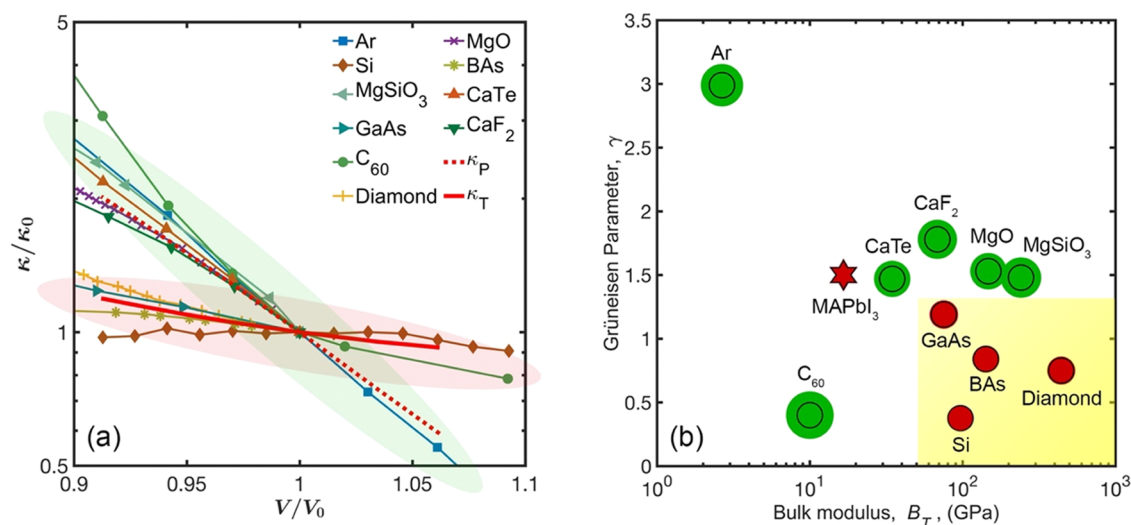
Figure 4. Pressure effect on the thermal conductivity for MAPbI$_3$ at 350 K and other materials (Ar at 20 K, others at room temperature from theoretical studies).[25,26,43−57] (a) Thermal conductivity as a function of volume with both normalized to their corresponding values at 0 GPa. (b) Grüneisen parameter (γ) and isothermal bulk modulus (B_T) for the materials in panel (a) at their corresponding temperatures and 0 GPa. The shaded area of each circle represents the squared value of κ/κ_0 from panel (a) at $V/V_0 = 0.95$. The thermal conductivity of stiff and weakly anharmonic materials (i.e., red color symbols) change minimally with compression, with no observable shaded area outside the original circle. The color of each circle corresponds to the material's location in panel (a).

channel thermal conductivity value into its two coupled phonon modes s and s'. The term in the round brackets is the coupled phonon lifetime between the two phonon modes, s and s'. This $D_A(\boldsymbol{q})_s$ contrasts with Allen−Feldman's harmonic modal diffusivity as the former includes anharmonicity.[35,36] Thus, the expression for $\kappa_C^\alpha(\boldsymbol{q})_s$ can be recast as

$$\kappa_C^\alpha(\boldsymbol{q})_s = C(\boldsymbol{q})_s D_A^\alpha(\boldsymbol{q})_s \tag{3}$$

In addition, we employ the average interband spacing (Δ_ω) to reflect the strength of κ_C.[20] Different from its original definition, $\Delta_\omega = \omega_{max}/3N$ in ref 20, we only focused on the low-frequency region to define ω_{max} and N as the contribution from phonons of frequencies higher than 6.5 THz is insignificant compared to phonons of lower frequencies (Figure S5). As shown in Figure 3b, the Δ_ω is almost constant, while the mode-averaged $D_A(\boldsymbol{q})_s$ fluctuates slightly around an average value as the pressure changes. These results suggest that the pressure effect on κ_C is negligible. The almost unchanged Δ_ω is due to the weak pressure effect on the MA cations that pins the highest intramolecular MA vibration[34] frequency responsible for ω_{max}. On the other hand, the nearly constant mode-averaged $D_A(\boldsymbol{q})_s$ suggests that the diffusivity from the wave-like transport in the coherence-channel is weakly affected by pressure. We postulate that the flat $D_A(\boldsymbol{q})_s$ curve arises from counteracting changes from the off-diagonal velocity and coupled phonon lifetime in eq 2. This postulation, however, requires further investigations to determine the physical origins of these off-diagonal group velocities and coupled phonon lifetimes.

To the best of our knowledge, little is known about the pressure effect on the coherence-channel contribution, κ_C. MAPbI$_3$ is suitable for such an investigation due to its dominant κ_C component.[21] We compared the thermal conductivity trend of some widely studied materials under pressure with that of MAPbI$_3$ in Figure 4. By normalizing with their intrinsic thermal conductivity under 0 GPa, these trends collapse into two distinct groups, as shown in Figure 4a. The normalized κ_T trend of c-MAPbI$_3$ under compression has a

gentle gradient, similar to materials in the red region. On the other hand, its normalized κ_P trend has a steeper gradient, similar to materials in the green region. For more insights, the Grüneisen parameter (γ) and isothermal bulk modulus (B_T) were used to gauge the strength of the anharmonicity[37] and the stiffness of the materials in Figure 4. These two factors are inputs to the Leibfried−Schlömann (LS) equation, $\kappa = AV^{1/3}\omega_D^3/(\gamma^2 T)$, commonly used to study the thermal conductivity of materials under pressure.[38,39] In this equation, A is a fitting parameter, V is the volume, T is the temperature, γ is the Grüneisen parameter, and ω_D is the acoustic Debye frequency. The bulk modulus at the pressure of interest enters the LS equation from the estimate of the Debye frequency through $\omega_D \propto V^{1/6}B_T^{1/2}$.[38] Thus, γ and B_T are appropriate for studying the pressure effect on thermal conductivity. The Grüneisen parameter is defined as[18,40]

$$\gamma = \frac{\sum_{\boldsymbol{q},s} \gamma(\boldsymbol{q})_s C(\boldsymbol{q})_s}{\sum_{\boldsymbol{q},s} C(\boldsymbol{q})_s} \tag{4}$$

where $\gamma(\boldsymbol{q})_s = -\partial \ln \omega(\boldsymbol{q})_s/\partial \ln V$. The isothermal bulk modulus is obtained from MD simulations using

$$B_T = -V\left(\frac{dP}{dV}\right)_T \tag{5}$$

where P is the pressure. Our calculated γ of 1.5 and B_T of 16.6 GPa for MAPbI$_3$ at $V/V_0 = 1.0$ (i.e., at the pressure of 0 GPa) agree with previous studies.[41,42] The γ and B_T at $V/V_0 = 1.0$ for other materials are taken from refs 25, 26, 43−57. Also, we separately confirmed that using γ and B_T calculated at a different pressure does not change our following conclusions (see Figure S6). The plot of γ versus B_T for various materials is shown in Figure 4b. We found that GaAs, BAs, Si, and diamond, whose thermal conductivity is less sensitive to compression (i.e., in the red region of Figure 4a) are considered weakly anharmonic (i.e., small γ) and stiff (i.e., large B_T). They occupy the yellow region in Figure 4b.[25,58] However, the other materials whose thermal conductivity

increases more significantly under compression (i.e., in the green region of Figure 4a) are often classified as strongly anharmonic (i.e., large γ) or/and soft (i.e., small B_T). They appear outside the yellow region in Figure 4b. For the strongly anharmonic and soft MAPbI$_3$, its normalized κ_P trend due to the phonon population-channel falls expectedly in the green region of Figure 4a. However, its normalized κ_T trend in Figure 4a fits into the red region and behaves like it is from a stiff and weakly anharmonic material. This behavior makes MAPbI$_3$ distinctive outside the yellow region in Figure 4b (i.e., red star). The underlying reason for this anomalous relationship is its invariant and dominant κ_C that overwhelms the gentle increase in the κ_P. This suppression, thus, makes the κ_T trend resilient, causing MAPbI$_3$ to respond like a stiff and weakly anharmonic material under low-to-moderate pressure.

3. CONCLUSIONS

In summary, the thermal transport properties of c-MAPbI$_3$ at pressures ranging from −0.8 to 2.0 Gpa are examined via the NEMD and PWTE using the MYP empirical potential. We discover that the coherence-channel thermal conductivity is nearly pressure-independent, while the population-channel thermal conductivity increases slightly with increasing pressure. The distinct responses of these two channels come from their phonon modal properties. Our results show that as the pressure increases, the average phonon group velocity and lifetime increase to produce more phonons with higher contributions to the population-channel. Further, we extracted an anharmonic modal diffusivity and modified the average interband spacing to elucidate the invariant coherence-channel trend. A comparison with other materials unveils an unusual thermal conductivity behavior in c-MAPbI$_3$ contributed by its invariant and dominant coherence-channel that suppresses its total thermal conductivity increase. This suppression imparts c-MAPbI$_3$ a resilient thermal conductivity trend under pressure, not found in other soft and/or strongly anharmonic materials. As existing literature has reported that pressure can effectively enhance the electronic properties of MAPbI$_3$, our result suggests that MAPbI$_3$ is a potential pressure-modulated thermoelectric material up to a pressure of 2 GPa, with decoupled electronic and thermal transport properties. However, in situations where changes to the thermal conductivity by an external field are favored, more research is needed to explore new ways to affect the coherence-channel contribution. Existing methods may be ineffective thermal transport regulators for materials with a dominant coherence-channel or wave-like thermal transport. Also, pressure studies of other complex crystals with sizeable coherence-channel contributions may reveal interesting but undiscovered transport physics and warrant further investigations.

4. METHODS

4.1. Nonequilibrium Molecular Dynamics (NEMD). LAMMPS[59] with the MYP empirical potential[12,60] was used to perform all MD simulations. The time step was 0.5 fs. A three-dimensional periodic system was simulated initially under an NPT ensemble for at least one nanosecond to reach the temperature of 350 K and the desired pressure. This system was then run in an NVT ensemble before relaxing in an NVE ensemble, each for a nanosecond. Following the relaxation, the system thermal conductivity was determined using a NEMD simulation with a four-unit-cell heat bath thermostated by a Langevin thermostat with a damping constant of 0.5 ps.[61,62] We found that a system with at least a cross-sectional area of 6 × 6 and a length of 400 conventional cubic unit cells was

required to avoid the finite-size effect. The temperature difference between the hot and cold reservoirs was within 15% of the system temperature. NEMD was run for 20 ns to reach a steady state before collecting data for calculating its thermal conductivity through the Fourier law. The standard deviation was computed using five independent runs with different initial seeds.

4.2. Structure Optimization. Cubic MAPbI$_3$ unit cells ($\alpha = \beta = \gamma$ = 90°) with 96 atoms were created for optimization. The lattice constants in all structures were averaged from an NPT ensemble at the desired pressure and the temperature of 350 K to account for thermal expansion and fixed during the structure optimization. As the common structural relaxation algorithm cannot find a stable c-MAPbI$_3$ configuration to generate positive phonon dispersion, we adopted a recently proposed two-step approach using commands in LAMMPS.[21] Here, preliminary energy minimization of the structures was first carried out using the conjugate gradient algorithm. Next, any remaining kinetic energy due to residual forces was dissipated using the "fix viscous" command.[59]

4.3. Interatomic Force Constants (IFCs) Extraction. The MYP potential[12,60] was used for the IFCs extraction in LAMMPS. We employ the finite-difference method[18] to calculate the second-order IFCs using a displacement of 0.001 Å. After subtracting the contributions of the second-order IFCs from the forces, the third-order IFCs were computed using the Taylor series fitting method.[18] Using the thermal stochastic snapshot technique,[58] the displaced structures at temperatures of 1 and 350 K were compared. The resulting over-specified force−displacement linear system was solved using the least-squares fit. We discover that for the two temperatures employed in the thermal stochastic snapshot technique, the difference in the predicted κ_T is within 6%. After convergence tests, the second-order and third-order IFCs cutoff of 10.00 and 5.05 Å and a converged phonon grid of 6 × 6 × 6 were selected.[21] Only three-phonon scattering under the single-mode relaxation time approximation was considered here.[63]

■ ASSOCIATED CONTENT

ⓢ Supporting Information

The Supporting Information is available free of charge at https://pubs.acs.org/doi/10.1021/acs.chemmater.3c00935.

Low pressure structures (ZIP)

Additional details on structures, phonon dispersions, phonon density of states, structural parameters, frequency-dependent cumulative thermal conductivity of MAPbI$_3$ at different pressures, and the effects of pressures on the Grüneisen parameter and isothermal bulk modulus of Ar, Si, and MAPbI$_3$ (PDF)

■ AUTHOR INFORMATION

Corresponding Author

Wee-Liat Ong − *ZJU-UIUC Institute, College of Energy Engineering, Zhejiang University, Haining, Zhejiang 314400, China; State Key Laboratory of Clean Energy Utilization, Zhejiang University, Hangzhou, Zhejiang 310027, China;* ⓞ orcid.org/0000-0003-3035-6991; Email: weeong@intl.zju.edu.cn

Authors

Jin Yang − *ZJU-UIUC Institute, College of Energy Engineering, Zhejiang University, Haining, Zhejiang 314400, China*

Ankit Jain − *Mechanical Engineering Department, IIT Bombay, Mumbai 400076, India;* ⓞ orcid.org/0000-0001-8091-9129

Liwu Fan − *State Key Laboratory of Clean Energy Utilization and Key Laboratory of Clean Energy and Carbon Neutrality of Zhejiang Province, Zhejiang University, Hangzhou,*

Zhejiang 310027, China; ⓞ orcid.org/0000-0001-8845-5058

Yee Sin Ang − *Science, Mathematics, and Technology, Singapore University of Technology and Design, Singapore 487372, Singapore;* ⓞ orcid.org/0000-0002-1637-1610

Hanying Li − *MOE Key Laboratory of Macromolecular Synthesis and Functionalization, International Research Center for X Poly-Mers, Department of Polymer Science and Engineering, Zhejiang University, Hangzhou 310027, China;* ⓞ orcid.org/0000-0002-5841-6805

Complete contact information is available at:
https://pubs.acs.org/10.1021/acs.chemmater.3c00935

Author Contributions

J.Y.: methodology, software, formal analysis, investigation, data curation, writing—original draft, and visualization. A.J.: methodology, software, validation, and writing—review and editing. L.-W.F.: resources and writing—review and editing. Y.S.A.: resources and writing—review and editing. H.L.: resources and writing—review and editing. W.-L.O.: conceptualization, methodology, resources, writing—review and editing, supervision, project administration, and funding acquisition.

Notes

The authors declare no competing financial interest.

■ REFERENCES

(1) Lin, R.; Xu, J.; Wei, M.; Wang, Y.; Qin, Z.; Liu, Z.; Wu, J.; Xiao, K.; Chen, B.; Park, S. M.; Chen, G.; Atapattu, H. R.; Graham, K. R.; Xu, J.; Zhu, J.; Li, L.; Zhang, C.; Sargent, E. H.; Tan, H. All-Perovskite Tandem Solar Cells with Improved Grain Surface Passivation. *Nature* **2022**, *603*, 73−78.

(2) Haque, M. A.; Kee, S.; Villalva, D. R.; Ong, W.; Baran, D. Halide Perovskites: Thermal Transport and Prospects for Thermoelectricity. *Adv. Sci.* **2020**, *7*, No. 1903389.

(3) Elbaz, G. A.; Ong, W.-L.; Doud, E. A.; Kim, P.; Paley, D. W.; Roy, X.; Malen, J. A. Phonon Speed, Not Scattering, Differentiates Thermal Transport in Lead Halide Perovskites. *Nano Lett.* **2017**, *17*, 5734−5739.

(4) Wang, Q.; Zeng, Z.; Zhao, P.; Chen, C.; Ouyang, N.; Mao, J.; Chen, Y. B-Site Columnar-Ordered Halide Double Perovskites: Breaking Octahedra Motions Induces Strong Lattice Anharmonicity and Thermal Anisotropy. *Chem. Mater.* **2023**, *35*, 1633−1639.

(5) Giri, A.; Thakur, S.; Mattoni, A. Molecular Rotor−Rotor Heat Diffusion at the Origin of the Enhanced Thermal Conductivity of Hybrid Perovskites at High Temperatures. *Chem. Mater.* **2022**, *34*, 9569−9576.

(6) Wang, M.; Ni, Z.; Xiao, X.; Zhou, Y.; Huang, J. Strain Engineering in Metal Halide Perovskite Materials and Devices: Influence on Stability and Optoelectronic Properties. *Chem. Phys. Rev.* **2021**, *2*, No. 031302.

(7) Jiao, Y.; Yi, S.; Wang, H.; Li, B.; Hao, W.; Pan, L.; Shi, Y.; Li, X.; Liu, P.; Zhang, H.; Gao, C.; Zhao, J.; Lu, J. Strain Engineering of Metal Halide Perovskites on Coupling Anisotropic Behaviors. *Adv. Funct. Mater.* **2021**, *31*, No. 2006243.

(8) Qiao, L.; Fang, W.-H.; Long, R.; Prezhdo, O. V. Elimination of Charge Recombination Centers in Metal Halide Perovskites by Strain. *J. Am. Chem. Soc.* **2021**, *143*, 9982−9990.

(9) Gao, Y.; Ning, W.; Zhang, X.; Liu, Y.; Zhou, Y.; Tang, D. The Effective Regulation of Nanotwinning on the Multichannel Thermal Transport in Hybrid Organic−Inorganic Halide Perovskite. *Nano Energy* **2021**, *82*, No. 105747.

(10) Giri, A. Origins of Pressure-Induced Enhancement in Thermal Conductivity of Hybrid Inorganic−Organic Perovskites. *Nanoscale* **2021**, *13*, 685−691.

(11) Rahman, M. A.; Giri, A. Uniquely Anisotropic Mechanical and Thermal Responses of Hybrid Organic−Inorganic Perovskites under Uniaxial Strain. *J. Chem. Phys.* **2021**, *155*, No. 124703.

(12) Mattoni, A.; Filippetti, A.; Saba, M. I.; Delugas, P. Methylammonium Rotational Dynamics in Lead Halide Perovskite by Classical Molecular Dynamics: The Role of Temperature. *J. Phys. Chem. C* **2015**, *119*, 17421−17428.

(13) Zhou, Y.; Dong, Z.-Y.; Hsieh, W.-P.; Goncharov, A. F.; Chen, X.-J. Thermal Conductivity of Materials under Pressure. *Nat. Rev. Phys.* **2022**, *4*, 319−335.

(14) Li, Y.; Liu, J.; Wang, X.; Hong, J. Anomalous Suppressed Thermal Conductivity in $CuInTe_2$ under Pressure. *Appl. Phys. Lett.* **2021**, *119*, No. 243901.

(15) Yuan, K.; Zhang, X.; Tang, D.; Hu, M. Anomalous Pressure Effect on the Thermal Conductivity of ZnO, GaN, and AlN from First-Principles Calculations. *Phys. Rev. B* **2018**, *98*, No. 144303.

(16) Xu, K.; Deng, S.; Liang, T.; Cao, X.; Han, M.; Zeng, X.; Zhang, Z.; Yang, N.; Wu, J. Efficient Mechanical Modulation of the Phonon Thermal Conductivity of Mo_6S_6 Nanowires. *Nanoscale* **2022**, *14*, 3078−3086.

(17) Yang, L.; Wan, X.; Ma, D.; Jiang, Y.; Yang, N. Maximization and Minimization of Interfacial Thermal Conductance by Modulating the Mass Distribution of the Interlayer. *Phys. Rev. B* **2021**, *103*, No. 155305.

(18) McGaughey, A. J. H.; Jain, A.; Kim, H.-Y. Phonon Properties and Thermal Conductivity from First Principles, Lattice Dynamics, and the Boltzmann Transport Equation. *J. Appl. Phys.* **2019**, *125*, No. 011101.

(19) Simoncelli, M.; Marzari, N.; Mauri, F. Unified Theory of Thermal Transport in Crystals and Glasses. *Nat. Phys.* **2019**, *15*, 809−813.

(20) Simoncelli, M.; Marzari, N.; Mauri, F. Wigner Formulation of Thermal Transport in Solids. *Phys. Rev. X* **2022**, *12*, No. 041011.

(21) Yang, J.; Jain, A.; Ong, W.-L. Inter-Channel Conversion between Population-/Coherence-Channel Dictates Thermal Transport in MAPbI3 Crystals. *Mater. Today Phys.* **2022**, *28*, No. 100892.

(22) Zhu, T.; Ertekin, E. Mixed Phononic and Non-Phononic Transport in Hybrid Lead Halide Perovskites: Glass-Crystal Duality, Dynamical Disorder, and Anharmonicity. *Energy Environ. Sci.* **2019**, *12*, 216−229.

(23) Wang, C.; Wang, Q.; Zhang, Q.; Chen, C.; Chen, Y. Intrinsic Zn Vacancies-Induced Wavelike Tunneling of Phonons and Ultralow Lattice Thermal Conductivity in Zintl Phase Sr_2ZnSb_2. *Chem. Mater.* **2022**, *34*, 7837−7844.

(24) Stackhouse, S.; Stixrude, L.; Karki, B. B. Thermal Conductivity of Periclase (MgO) from First Principles. *Phys. Rev. Lett.* **2010**, *104*, No. 208501.

(25) Parrish, K. D.; Jain, A.; Larkin, J. M.; Saidi, W. A.; McGaughey, A. J. H. Origins of Thermal Conductivity Changes in Strained Crystals. *Phys. Rev. B* **2014**, *90*, No. 235201.

(26) Ravichandran, N. K.; Broido, D. Non-Monotonic Pressure Dependence of the Thermal Conductivity of Boron Arsenide. *Nat. Commun.* **2019**, *10*, No. 827.

(27) Li, S.; Qin, Z.; Wu, H.; Li, M.; Kunz, M.; Alatas, A.; Kavner, A.; Hu, Y. Anomalous Thermal Transport under High Pressure in Boron Arsenide. *Nature* **2022**, *612*, 459−464.

(28) Ge, C.; Hu, M.; Wu, P.; Tan, Q.; Chen, Z.; Wang, Y.; Shi, J.; Feng, J. Ultralow Thermal Conductivity and Ultrahigh Thermal Expansion of Single-Crystal Organic−Inorganic Hybrid Perovskite $CH_3NH_3PbX_3$ (X = Cl, Br, I). *J. Phys. Chem. C* **2018**, *122*, 15973−15978.

(29) Momma, K.; Izumi, F. *VESTA 3* for Three-Dimensional Visualization of Crystal, Volumetric and Morphology Data. *J. Appl. Crystallogr.* **2011**, *44*, 1272−1276.

(30) Gu, H.; Wang, H. Effect of Strain on Thermal Conductivity of Amorphous Silicon Dioxide Thin Films: A Molecular Dynamics Study. *Comput. Mater. Sci.* **2018**, *144*, 133−138.

(31) Pisoni, A.; Jaćimović, J.; Barišić, O. S.; Spina, M.; Gaál, R.; Forró, L.; Horváth, E. Ultra-Low Thermal Conductivity in Organic−Inorganic Hybrid Perovskite $CH_3NH_3PbI_3$. *J. Phys. Chem. Lett.* **2014**, *5*, 2488−2492.

(32) Feng, T.; Ruan, X. Quantum Mechanical Prediction of Four-Phonon Scattering Rates and Reduced Thermal Conductivity of Solids. *Phys. Rev. B* **2016**, *93*, No. 045202.

(33) Amat, A.; Mosconi, E.; Ronca, E.; Quarti, C.; Umari, P.; Nazeeruddin, M. K.; Grätzel, M.; De Angelis, F. Cation-Induced Band-Gap Tuning in Organohalide Perovskites: Interplay of Spin−Orbit Coupling and Octahedra Tilting. *Nano Lett.* **2014**, *14*, 3608−3616.

(34) Yue, S.-Y.; Zhang, X.; Qin, G.; Yang, J.; Hu, M. Insight into the Collective Vibrational Modes Driving Ultralow Thermal Conductivity of Perovskite Solar Cells. *Phys. Rev. B* **2016**, *94*, No. 115427.

(35) Allen, P. B.; Feldman, J. L. Thermal Conductivity of Glasses: Theory and Application to Amorphous Si. *Phys. Rev. Lett.* **1989**, *62*, 645−648.

(36) Allen, P. B.; Feldman, J. L.; Fabian, J.; Wooten, F. Diffusons, Locons and Propagons: Character of Atomie Yibrations in Amorphous Si. *Philos. Mag. B* **1999**, *79*, 1715−1731.

(37) Fabian, J.; Allen, P. B. Thermal Expansion and Grüneisen Parameters of Amorphous Silicon: A Realistic Model Calculation. *Phys. Rev. Lett.* **1997**, *79*, 1885−1888.

(38) Chen, B.; Hsieh, W.-P.; Cahill, D. G.; Trinkle, D. R.; Li, J. Thermal Conductivity of Compressed H_2O to 22 GPa: A Test of the Leibfried-Schlömann Equation. *Phys. Rev. B* **2011**, *83*, No. 132301.

(39) Dalton, D. A.; Hsieh, W.-P.; Hohensee, G. T.; Cahill, D. G.; Goncharov, A. F. Effect of Mass Disorder on the Lattice Thermal Conductivity of MgO Periclase under Pressure. *Sci. Rep.* **2013**, *3*, No. 2400.

(40) Ashcroft, N. W.; Mermin, N. D. *Solid State Physics*; Saunders College Publishing: Fort Worth, 1976.

(41) Brivio, F.; Frost, J. M.; Skelton, J. M.; Jackson, A. J.; Weber, O. J.; Weller, M. T.; Goñi, A. R.; Leguy, A. M. A.; Barnes, P. R. F.; Walsh, A. Lattice Dynamics and Vibrational Spectra of the Orthorhombic, Tetragonal, and Cubic Phases of Methylammonium Lead Iodide. *Phys. Rev. B* **2015**, *92*, No. 144308.

(42) Rakita, Y.; Cohen, S. R.; Kedem, N. K.; Hodes, G.; Cahen, D. Mechanical Properties of APbX3 (A = Cs or CH3NH3; X= I or Br) Perovskite Single Crystals. *MRS Commun.* **2015**, *5*, 623−629.

(43) Tian, F.; Luo, K.; Xie, C.; Liu, B.; Liang, X.; Wang, L.; Gamage, G. A.; Sun, H.; Ziyaee, H.; Sun, J.; Zhao, Z.; Xu, B.; Gao, G.; Zhou, X.-F.; Ren, Z. Mechanical Properties of Boron Arsenide Single Crystal. *Appl. Phys. Lett.* **2019**, *114*, No. 131903.

(44) Chen, X.; Li, C.; Tian, F.; Gamage, G. A.; Sullivan, S.; Zhou, J.; Broido, D.; Ren, Z.; Shi, L. Thermal Expansion Coefficient and Lattice Anharmonicity of Cubic Boron Arsenide. *Phys. Rev. Appl.* **2019**, *11*, No. 064070.

(45) Lundin, A.; Sundqvist, B.; Skoglund, P.; Fransson, A.; Pettersson, S. Compressibility, Specific Heat Capacity, and Gr[ineisen Parameter For C60/c70. *Solid State Commun.* **1992**, *84*, 879−883.

(46) Kolomenskii, A. A.; Szabadi, M.; Hess, P. Laser Diagnostics of C60 and C70 Films by Broadband Surface Acoustic Wave Spectroscopy. *Appl. Surf. Sci.* **1995**, *86*, 591−596.

(47) Ehrenreich, H.; Hirth, J. P. Mechanism for Dislocation Density Reduction in GaAs Crystals by Indium Addition. *Appl. Phys. Lett.* **1985**, *46*, 668−670.

(48) Wickboldt, P.; Anastassakis, E.; Sauer, R.; Cardona, M. Raman Phonon Piezospectroscopy in GaAs: Infrared Measurements. *Phys. Rev. B* **1987**, *35*, 1362−1368.

(49) Liu, Z.-j.; Sun, X.; Zhang, C.; Hu, J.; Song, T.; Qi, J. Elastic Tensor and Thermodynamic Property of Magnesium Silicate Perovskite from First-Principles Calculations. *Chin. J. Chem. Phys.* **2011**, *24*, 703−710.

(50) Keeler, G. J.; Batchelder, D. N. Measurement of the Elastic Constants of Argon from 3 to 77 Degrees K. *J. Phys. C: Solid State Phys.* **1970**, *3*, 510−522.

(51) Nath, P.; Plata, J. J.; Usanmaz, D.; Al Rahal Al Orabi, R.; Fornari, M.; Nardelli, M. B.; Toher, C.; Curtarolo, S. High-Throughput Prediction of Finite-Temperature Properties Using the Quasi-Harmonic Approximation. *Comput. Mater. Sci.* **2016**, *125*, 82−91.

(52) Giri, A.; Hopkins, P. E. Pronounced Low-Frequency Vibrational Thermal Transport in C_{60} Fullerite Realized through Pressure-Dependent Molecular Dynamics Simulations. *Phys. Rev. B* **2017**, *96*, No. 220303.

(53) Sun, Z.; Yuan, K.; Zhang, X.; Tang, D. Pressure Tuning of the Thermal Conductivity of Gallium Arsenide from First-Principles Calculations. *Phys. Chem. Chem. Phys.* **2018**, *20*, 30331−30339.

(54) Ghaderi, N.; Zhang, D.-B.; Zhang, H.; Xian, J.; Wentzcovitch, R. M.; Sun, T. Lattice Thermal Conductivity of MgSiO3 Perovskite from First Principles. *Sci. Rep.* **2017**, *7*, No. 5417.

(55) Broido, D. A.; Lindsay, L.; Ward, A. Thermal Conductivity of Diamond under Extreme Pressure: A First-Principles Study. *Phys. Rev. B* **2012**, *86*, No. 115203.

(56) Faraji, S.; Allaei, S. M. V.; Amsler, M. Thermal Conductivity of CaF_2 at High Pressure. *Phys. Rev. B* **2021**, *103*, No. 134301.

(57) Yang, Z.; Yuan, K.; Meng, J.; Zhang, X.; Tang, D.; Hu, M. Why Thermal Conductivity of CaO Is Lower than That of CaS: A Study from the Perspective of Phonon Splitting of Optical Mode. *Nanotechnology* **2021**, *32*, No. 025709.

(58) Ravichandran, N. K.; Broido, D. Unified First-Principles Theory of Thermal Properties of Insulators. *Phys. Rev. B* **2018**, *98*, No. 085205.

(59) Thompson, A. P.; Aktulga, H. M.; Berger, R.; Bolintineanu, D. S.; Brown, W. M.; Crozier, P. S.; in't Veld, P. J.; Kohlmeyer, A.; Moore, S. G.; Nguyen, T. D.; Shan, R.; Stevens, M. J.; Tranchida, J.; Trott, C.; Plimpton, S. J. LAMMPS - a Flexible Simulation Tool for Particle-Based Materials Modeling at the Atomic, Meso, and Continuum Scales. *Comput. Phys. Commun.* **2022**, *271*, No. 108171.

(60) Mattoni, A.; Filippetti, A.; Caddeo, C. Modeling Hybrid Perovskites by Molecular Dynamics. *J. Phys.: Condens. Matter* **2017**, *29*, No. 043001.

(61) Li, Z.; Xiong, S.; Sievers, C.; Hu, Y.; Fan, Z.; Wei, N.; Bao, H.; Chen, S.; Donadio, D.; Ala-Nissila, T. Influence of Thermostatting on Nonequilibrium Molecular Dynamics Simulations of Heat Conduction in Solids. *J. Chem. Phys.* **2019**, *151*, No. 234105.

(62) Chen, W.-J.; Feng, B.; Shao, C.; Yang, J.; Fan, L.; Ong, W.-L.; Chang, I.-L. Asymmetrical Carbon Nanotubes Exhibit Opposing Thermal Rectification Behaviors under Different Heat Baths. *Int. J. Heat Mass Transfer* **2022**, *184*, No. 122341.

(63) Turney, J. E.; Landry, E. S.; McGaughey, A. J. H.; Amon, C. H. Predicting Phonon Properties and Thermal Conductivity from Anharmonic Lattice Dynamics Calculations and Molecular Dynamics Simulations. *Phys. Rev. B* **2009**, *79*, No. 064301.